THE ASTROPHYSICAL JOURNAL, 458:817–831, 1996 February 20

THE LARGE-SCALE DENSITY STRUCTURE OF THE SOLAR CORONA AND THE HELIOSPHERIC CURRENT SHEET

MADHULIKA GUHATHAKURTA[1]
NASA, Goddard Space Flight Center, Code 682, Greenbelt, MD 20771
THOMAS E. HOLZER
High Altitude Observatory, National Center for Atmospheric Research, P.O. Box 3000, Boulder, CO 80307
AND
R. M. MACQUEEN
Department of Physics, Rhodes College, 2000 North Parkway, Memphis, TN 38112
Received 1992 July 2; accepted 1995 August 22

ABSTRACT

We have investigated the three-dimensional distribution of the polarization-brightness product (pB) and then quantitatively determined the electron density distribution relative to the inferred heliographic current sheet during the declining phase of solar cycle 20 (1973–1976). The current sheet is taken as the center of the bright, dense structures from combined synoptic pB data from ground-based K-coronameter and the white-light coronagraph aboard *Skylab*. Analyses of pB scans as a function of minimum distance from the current sheet (θ_{min}) over the radial distance range 1.13 to 5.0 $R_\odot$ (from Sun center) led to the following new results: (1) a quantitative description of pB obtained around the inferred neutral line is given by the following equation:

$$pB(\rho, \theta_{min}) = pB_p(\rho) + [pB_{cs}(\rho) - pB_p(\rho)]e^{-\theta_{min}^2/w^2(r)} ,$$

where ρ is the shortest distance to the line of sight from the Sun center, $pB_{cs}(\rho)$ and $pB_p(\rho)$ are the observed polarized brightness at the current sheet and the poles, respectively, and $w(r)$ is the half-width of the distribution; (2) the electron density obtained by inverting the pB data is given by

$$N(r, \theta_{mg}) = N_p(r) + [N_{cs}(r) - N_p(r)]e^{-\theta_{mg}^2/w^2(r)} ,$$

where $N(r, \theta_{mg})$ is the number of free electrons per cm^3, $N_{cs}(r)$ and $N_p(r)$ are the electron densities at the current sheet and the poles, respectively, and θ_{mg} is the magnetic latitude. Here θ_{mg} is given by

$$\theta_{mg} = \sin^{-1} [-\cos \theta \sin \alpha \sin (\phi - \phi_0) + \sin \theta \cos \alpha] ,$$

where θ and ϕ are heliographic latitude and longitude, α is the tilt angle of the dipole axis with the rotation axis, and ϕ_0 is the intersecion of the heliomagnetic and heliographic equators; (3) during the period studied (the last third of the solar cycle), the mean pB at the current sheet and above the polar holes is approximately independent of the phase of the solar cycle; and (4) the organization of pB data about the neutral line allows inference of the boundary of the polar coronal holes.

The usefulness of one-dimensional white-light density constraint in solar wind modeling has already been demonstrated by Habbal et al. The present three-dimensional model should prove very useful in better understanding of the global hydromagnetic structure of the corona and the solar wind, relating as it does to the magnetic structure of the corona, as opposed to heliocentric coordinates. For example, the density model could provide constraints on coronal temperature, flow velocity, and magnetic structure subject to a suitable analysis of geometric effects, which in turn would provide constraints on energy balance in the coronal expansion.

Subject headings: Sun: corona — Sun: magnetic fields

1. INTRODUCTION

It has been known for some time that the large-scale geometry of the coronal magnetic fields plays an important role in shaping the brightness distributions of the white-light corona. Specifically, the presence of expansion caused by the solar wind divides the corona into magnetically "open" and "closed" regions. Near solar minimum, the corona tends to be dim near the poles and bright near the equator; the bright regions tend to coincide with large loop (closed magnetic geometry) structures or helmet streamers, while the dim regions are associated with polar coronal holes (open magnetic geometry).

Coronal holes, which play an important role in describing the global structure of the coronal and interplanetary magnetic fields, are known to be regions of low density, associated with diverging, open magnetic field lines with a dominant magnetic polarity overlying areas of the photosphere with the same polarity (Zirker 1977). This open coronal magnetic field (Levine 1977) allows the coronal plasma to expand as a high-speed solar wind stream (Hundhausen 1977). The oppositely directed magnetic fields and the flow from the north and south polar coronal holes divide the heliospheric plasma into

[1] Also at the Physics Department, The Catholic University of America, Washington, DC.

roughly two regions (of opposite magnetic polarity) separated by a surface called the neutral sheet (Schultz 1973) or the current sheet. Although the current sheet constitutes a natural surface of symmetry for the propagation of heliospheric plasma, only a few phenomenological studies (Howard & Koomen 1974; Hundhausen 1977; Wilcox & Hundhausen, 1983; Bruno, Burlaga, & Hundhausen 1984) have examined the spatial variation of the brightness structure in the quiet K corona (or large-scale corona) relative to the current sheet. In this paper we establish an empirical model of the large-scale electron density with respect to the current sheet inferred from the product of coronal polarization and brightness (pB) measurements from the K-coronameter. A current sheet defined in this manner has been found consistent with that deduced from surface magnetic field measurements (see § 2.3).

A large body of research has been devoted to modeling the electron density in the corona. The primary source of information concerning the distribution of electron density is derived from electron scattering theory (van de Hulst 1950; Billings 1966) as applied to white-light observations. Traditionally, the electron density has been modeled as a function of radial distance r from the Sun center. Models applicable to the period of solar maximum activity are derived under the assumption of spherical symmetry; thus, a single function of r describes the density distribution of the entire corona. Models for solar minimum activity, on the other hand, assume azimuthal symmetry, and thus they involve both equatorial and polar models, each of which is a function of r only. A significant number of spherically symmetric models of the corona have been reviewed by Shklovskii (1965), Billings (1966), and Newkirk (1967). Subsequently, Saito (1970) developed an axisymmetric model of the solar minimum corona using data from several eclipses and the K-coronameter. A systematic procedure to determine the electron density of the inner corona (for a 14 day period) involving no assumption of coronal symmetry has been provided by Altschuler & Perry (1971) and Perry & Altschuler (1973) using data from the K-coronameter, although the uniqueness of the resulting density model has not been established. White-light coronagraph data from *Skylab* were used by Saito, Poland, & Munro (1977) to obtain an axisymmetric equatorial and polar model of the preminimum corona and, using data (for a period of 14 days) from *Skylab*, Munro & Jackson (1977, hereafter MJ) developed an axisymmetric model of polar coronal hole.

All the above empirical models (barring the Perry & Altschuler model) are based on the assumption of either spherical or azimuthal symmetry of the corona, with the equatorial plane of the Sun assumed to be the surface of symmetry.

This paper describes the physically more realistic situation in which the coronal electron density is shown to be a function of the large-scale *magnetic* geometry. We obtain an empirical model for the electron density as a function of r and angular distance θ_{mg}, from a current sheet that results from a titled dipole axis where as observationally the neutral line is inferred from the band of maximum brightness of pB data. The study is based on observations of the white-light corona made with the K-coronameter at the Mauna Loa Observatory (1973–1976) (1.12–2.0 $R_\odot$) and the White-Light Coronagraph aboard *Skylab* (1973–1974) (2.5–5.5 $R_\odot$). We employ both data sets to obtain a three-dimensional density model of the corona (from 1.2–5 $R_\odot$) during the period 1973–1974, a period when coronal structure was rather simple and relatively unchanging. After a brief description of the data, their display, and their limitations in the study of coronal electron density, we will describe both qualitatively and quantitatively a simple pattern of organization based on the inferred current sheet.

2. OBSERVATIONS AND DATA ANALYSIS

2.1. *White-Light Corona*

The dominant source of the white-light corona is scattered photospheric light. The light scattered by electrons gives rise to the K corona, while light scattered by dust particles gives rise to the F corona, or Fraunhofer corona. We employ three different data sets. The polarization brightness product, pB (the difference in the intensity of white-light coronal radiation polarized along the direction radial to the Sun and tangential to the limb of the sun) observations, taken by the High Altitude Observatory (HAO) K-coronameter at Mauna Loa; pB observations from the white-light coronagraph aboard *Skylab*; and pB observations from the HAO coronal eclipse camera. The three data sets used have been discussed extensively in the literature. Therefore, we outline these sets only briefly and provide appropriate references detailing the instrumentation and data reduction techniques.

2.1.1. *K-Coronameter, White-Light Coronagraph, and Inner Coronal Camera*

The Mark II K-coronameter collected data from 1969 May to 1978 September. This instrument measured pB around the occulted limb of the Sun at a series of heights between 1.12 and 2.0 $R_\odot$, at an effective wavelength of 6300 Å. Data were calibrated relative to the disk center brightness ($I_\odot$). This instrument has been described by Wilson (1977). K-coronameter data are taken as scans over position angle at various heights in the plane of the sky, and then converted into heliographic coordinates.

The HAO's white-light coronagraph (WLC) aboard *Skylab* obtained photographic coronal images through one unpolarized and three linearly polarized filters around the occulted limb of the Sun with a field of view between 2.0 and 5.5 $R_\odot$ during the period of 1973 May to 1974 February (MacQueen et al. 1974). The coronagraph data were calibrated relative to the mean brightness of the disk ($B_\odot$) at an effective wavelength of 5200 Å. The polarization brightness product, pB, is calculated from the combination of images obtained through three polaroid filters at different orientations. For details of these data and their reduction, see MacQueen et al. (1974), Wilson (1977), and Guhathakurta (1989).

The HAO's coronal camera observed the solar corona in white light during the total solar eclipse of 1973 June 30. The camera took measurements of the brightness and the polarized brightness of the corona. The data were calibrated relative to the mean brightness of the disk ($B_\odot$) at an effective wavelength of 6500 Å. A detailed description of the instrument can be found in a technical report by Lilliquist (1977).

2.1.2. *Display and Cross Calibration of Mark II and WLC Data*

Daily scans of pB data from Mark II are stored as a function of heliographic latitude (measured from heliographic north) for a given height. This sequence of data is then displayed as a "synoptic map" of pB data which is a function of solar latitude θ and the Carrington longitude L. In Figure 1 we present contour maps of pB (θ, L) derived from the daily scans taken at height 1.5 $R_\odot$ above the east limb. Each individual map represents one Carrington rotation. Solar longitude (or time) is

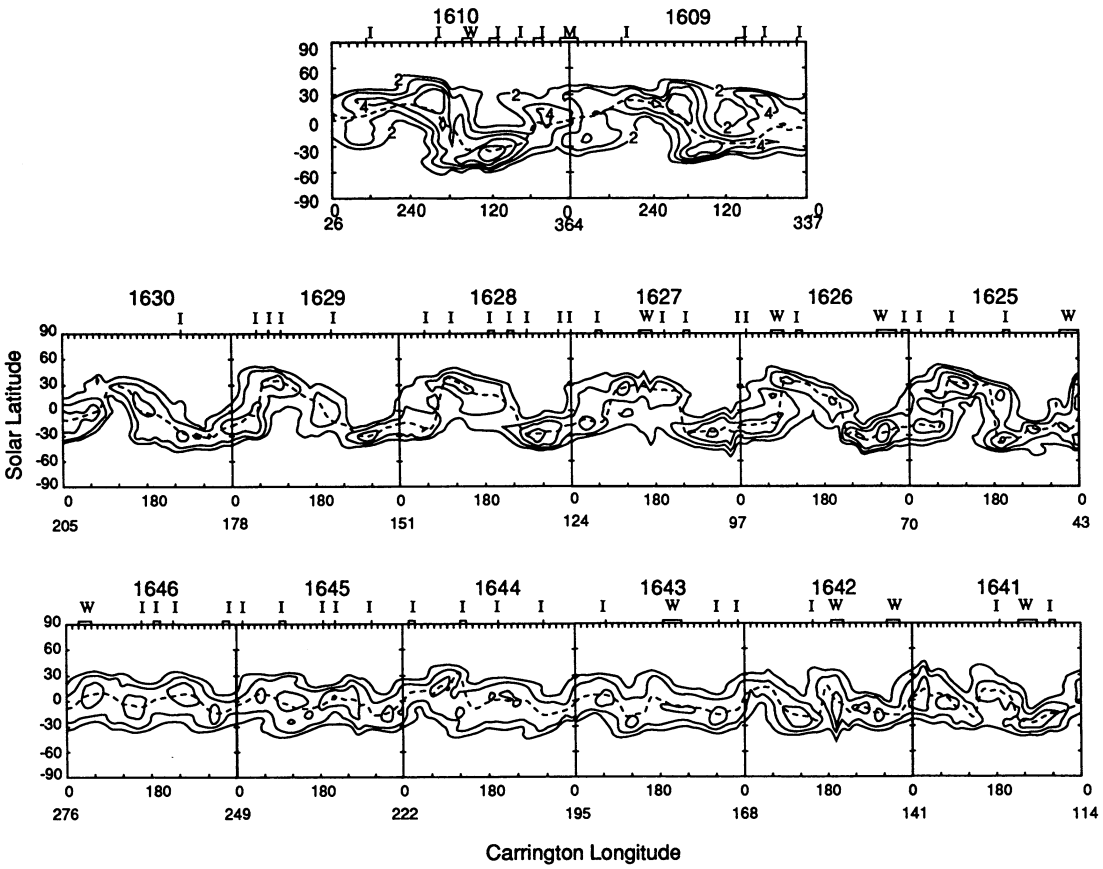

FIG. 1.—Synoptic maps of pB measured in original units of Mark II, $10^{-8} I_{\odot}$ (6300 Å), based on east limb observations at 0.5 $R_{\odot}$ above the limb consisting of 2–6 Carrington rotations (labeled by number at top of each map) for epochs 1, 2, and 3. The dashed line at the center of the streamer represents the neutral line for each rotation. Contours of brightness at the levels 2, 3, 4 × $10^{-8} I_{\odot}$ (6300 Å) (units of Mark II) have been generated from values measured at the intersections of the "observing grid" shown. These positions are spaced 1 day in longitude (the begin and end days are marked at the lower right- and left-hand corners, respectively) and 5° in solar latitude.

used as the unit of measure along the abscissa. The pB values are spaced 5° in latitude and 1 day (where 27.3 days correspond to a solar rotation) in longitude. The contours of pB are determined from the values measured on the grid θ_i and L_i.

Two interpolation techniques were applied to fill in gaps resulting from missing data. Whenever data from a single day or two consecutive days were missing, a linear or a cubic interpolation was carried out respectively (those are marked by the symbol I for the appropriate longitude along the upper margin of each synoptic map). Any data gaps for three or more days on the east limb are filled in based on the west limb observations half a solar rotation later (these are marked by the symbol W for the appropriate longitude along the upper margin of each synoptic map).

We utilized Mark II pB measurements taken at heights 1.12–2.0 $R_{\odot}$ above the east limb of the Sun and for every 5° in latitude. Since Mark II took only one observation per 24 hr period, the minimum detectable longitudinal separation of structures was 2 days' solar rotation or about 26° longitude as viewed from the Earth (Fisher et al. 1985).

The reduced pB data from WLC were presented in a similar "synoptic map" format for the entire *Skylab* period (Munro 1985) for heights 2.5–5.0 $R_{\odot}$. Except for three gaps of several days (1973 June 10–18, July 16–28, and November 15–17), the data set permitted calculation of pB at the rate of at least once a day from 1973 May 28 to 1974 February 11. In order to be consistent with the Mark II data set, we used only one set of WLC pB observations per 24 hr period for every 5° in latitude along the east limb of the Sun at each height.

Both Mark II and WLC data are used to construct an electron density model of the corona from 1.12 to 5.0 $R_{\odot}$; hence, a cross-calibration of the two instruments is required. Unfortunately, a direct cross-calibration between these two data sets was not possible owing to the lack of overlapping fields of view. It is, however, possible to compare the Mark II and WLC observations with observations obtained by the HAO white-light coronal camera. Guhathakurta (1989) describes this procedure, which results in multiplying the Mark II data by a factor of 2.18 to agree with the WLC data set.

2.2. *Selection of Epochs*

During the last third of 1973 through mid-1975, the corona exhibited a simple structure that evolved slowly with time. During this period, the corona was dominated by two prominent polar holes. It has been suggested (Hundhausen 1977) that this coronal structure could be described by a neutral line (where the radial component of the magnetic field $B_r = 0$) in the outer corona, tilted at an angle of 30° ± 5° to the solar equator. But conditions changed with the approach of solar minimum around 1976 June, when the angle of inclination

decreased to $15° \pm 5°$ (Guhathakurta 1989; Zhao & Hundhausen 1983).

Given these slowly varying conditions, it is possible to construct reasonably representative synoptic pB maps over an extended time period, as illustrated in Figure 1. For our model, we require slow evolution reflected in the synoptic maps by successive maps showing only small changes in the major features of interest. Based on this criterion, three epochs were selected during the period 1973–1976, corresponding to the descending phase of the solar cycle 20: epoch 1 (1973 day of year [DOY] 337 to 1974 DOY 026, Carrington rotations 1609–1610), and epochs 2 and 3, corresponding, respectively, to the beginning (1975 DOY 043 to 1975 DOY 205, Carrington rotations 1625–1630) and the end (1976 DOY 114 to 1976 DOY 276, Carrington rotations 1641–1646) of the solar minimum period.

The main feature of interest in each of the maps is the sinusoidal band of bright corona that changes gradually from rotation to rotation. This band feature represents the real, slowly varying large-scale spatial structure. The detailed shapes of smaller features, such as the low-brightness regions near 120° and 240° Carrington longitudes in Figure 1, epoch 1, and near 130° and 270° Carrington longitudes in epoch 2, show greater changes.

For epochs 1, 2, and 3, respectively, 27%, 28%, and 24% of the K-coronameter data are interpolated. WLC data are available only for epoch 1 but are complete.

2.3. *The Heliospheric Current Sheet*

We assume a simple model of the heliospheric magnetic field in which there is an Archimedian spiral field directed in one direction above the current sheet and in the other direction below the current sheet. The current sheet itself is taken to be the outward extension (by the solar wind) of a surface, which at the Sun is a plane inclined at an angle α to the solar equator resulting in two magnetic sectors being observed at 1 AU, within an angle α of the heliographic equator. Observational evidence supports this basic picture of the magnetic field during the period 1973–1976 (Jokipii & Thomas 1981; Thomas & Smith 1981; Zhao & Hundhausen 1981). Thus, the simplest model of a current sheet is one in which the current sheet approaches a planar surface as $r \to 1\ R_\odot$, with the magnetic plane being at an angle α relative to the solar equatorial plane. Assuming a constant and radial solar wind velocity V_w, Jokipii et al. (1981) showed that for $r > 1\ R_\odot$, the current sheet satisfies the equation

$$\theta = \pi/2 + \sin^{-1}\left[\sin\alpha \sin\left(\phi - \phi_0 + r\Omega_\odot/V_w\right)\right], \quad (1)$$

where r, θ, and ϕ are spherical polar coordinates relative to the solar rotation axis, α is the tilt angle, and $\Omega_\odot$ is the angular rotational velocity of the Sun.

Two approaches—one based upon using the centroid of the bright, white-light (pB) corona, and the other upon the potential extrapolation of measured surface magnetic fields—have been devised to determine the position of the neutral line. Both assume that beyond a certain height r, the coronal current sheet is swept out radially to form the interplanetary current sheet and that no interaction between streams of different speed occurs. Hansen, Sawyer, & Hansen (1974) first showed the correlation between observed coronal streamer patterns and sector boundaries observed at 1 AU. Howard & Koomen (1974), using *OSO 7* coronagraph measurements from 1972–1973, demonstrated a strong correlation between the observed bright corona and the 1 AU interplanetary magnetic field pattern. An empirical method was suggested by Hundhausen (1977) in which the coronal neutral line in the corona (above $2\ R_\odot$) was identified with the brightest or densest regions of the inner corona as observed in K-coronameter synoptic maps.

In the second approach (theoretical), Pneuman, Hansen, & Hansen (1978) used the low spatial resolution observations of the line-of-sight photospheric magnetic field to provide the boundary conditions for a calculation of the potential field on an outer coronal "source surface" (following ideas originally developed by Altschuler & Newkirk [1969] and Schatten, Wilcox, & Ness [1969]). The intersection of the current sheet with the source surface corresponds to the neutral line at which the radial component of the magnetic field (B_r) was zero. Pneuman et al. (1978) found the general correspondence between bright regions in the K corona and the computed closed field regions to be in good agreement with the computed neutral lines lying at the top of the closed loops. The two approaches have been compared, and several studies have suggested that the inference of the position of the current sheet from the K coronal data is more precise than from the magnetic potential field calculation (Pneuman et al. 1978; Thomas et al. 1981; Bruno et al. 1982; Behanon, Burlaga, & Hundhausen 1983). However, subsequent analyses (Hoeksema, Wilcox, & Scherrer 1982; Wilcox & Hundhausen 1983; Hoeksema 1984) suggest that the excessively large amplitude excursions of the current sheet resulting from the potential field model may well be a consequence of the imprecise determination of the photospheric fields in the polar regions. Recently Wang & Sheely (1992) suggested that magnetograph measurements apply to deep atmospheric layers in which the magnetic field is nonpotential (for observations made in the Fe I λ5250 line) and nearly radial. Hence, they matched only the radial component of the potential field to the photospheric field divided by $\sin\theta$ (in order to correct for the line-of-sight projection effect). This method produced a neutral line that is consistent with the neutral line determined from the brightness regions in the K corona. By contrast, the line-of-sight technique yields a neutral line extending to much higher latitudes than indicated by the observations.

In this analysis, we employ synoptic K coronameter observations for the inner and middle corona and the WLC data for the outer corona and assume that the coronal neutral line falls in the middle of the "streamer belt" defined by the boundaries of the northern and southern polar coronal holes (Guhathakurta 1989), at least during the descending and minimum phase of cycle 20.

The changes in the coronal polarized brightness and hence the neutral line profile for a typical rotation as a function of height above the limb, is depicted in Figure 2 for epoch 1. Note that bright coronal regions have decreasing angular widths at increasing heights (an observation that was made earlier by Hundhausen 1977), ultimately narrowing in the outer corona in a manner similar to the boundaries of coronal streamers seen in eclipse photographs (see Newkirk 1972). The neutral line geometry which follows the coronal pB changes gradually with radial distance, the profile becoming simpler (fewer distortions) and more nearly sinusoidal with increasing height. From examinations of epochs 1, 2, and 3, we conclude that the neutral line geometry for all heights greater than $1.5\ R_\odot$ remains practically (within a variation of $\pm 10\%$ of the neutral line at 1.5) the same in terms of latitudinal displacement from the equator.

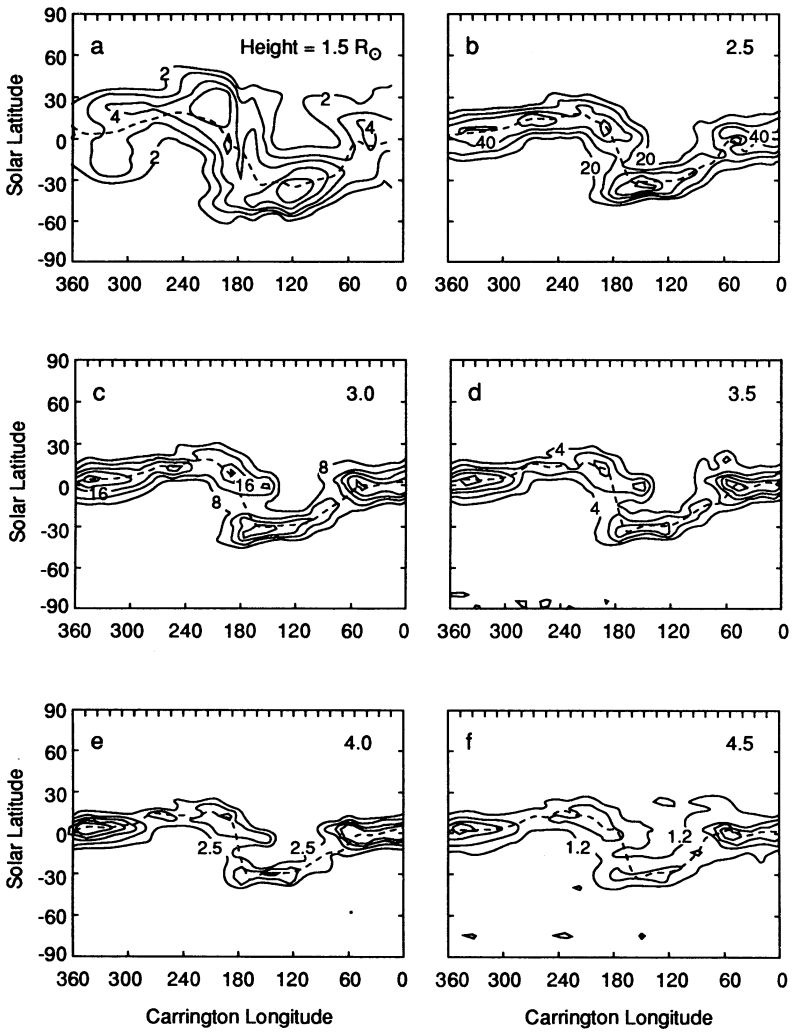

FIG. 2.—Synoptic maps of pB at height (*a*) 1.5 $R_\odot$ in Mark II units of 10^{-8} $I_\odot$ (6300 Å) and pB measured in original units of ATM data set, where contour levels range from 60. × 10^{-10} to 1.2 × 10^{-10} $B_\odot$ (5200 Å), at heights of (*b*) 2.5, (*c*) 3.0, (*d*) 3.5, (*e*) 4.0, and (*f*) 4.5 $R_\odot$ for Carrington rotation 1610, 1974. The dashed line at the center of the streamer represents the neutral line for each rotation.

2.4. *Angular Separation Between a Coronal Source and the Current Sheet*

If the dipole axis is tilted at an angle α with respect to the rotation axis of the Sun, then the heliomagnetic equatorial plane (the current sheet is contained in this plane) is tilted at an angle α with respect to the equatorial plane of the Sun. The heliomagnetic equator (neutral line) appears as the curve in Figure 3 in the planar (in terms of heliographic latitude and longitude) projection of the solar surface at a given height. In the heliomagnetic coordinate system, the separation between a coronal source and the current sheet is given by the heliomagnetic latitude θ_{mg}. For a given coronal source at heliographic latitude θ and longitude ϕ, the heliomagnetic latitude is given by

$$\sin \theta_{mg} = -\cos \theta \sin \alpha \sin (\phi - \phi_0) + \sin \theta \cos \alpha , \quad (2)$$

where ϕ_0 is the longitude of intersection of the heliomagnetic and heliographic equators. In Figure 3, we have chosen ϕ_0 to be equal to 0°.

Since the neutral line profiles obtained from the synoptic maps of pB bear some resemblance to the curve in Figure 3 but

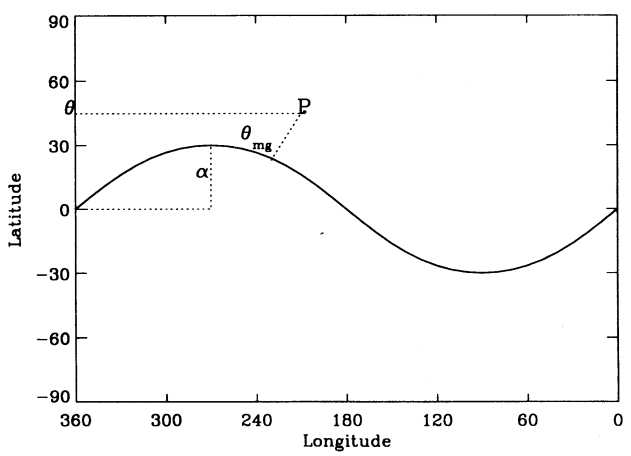

FIG. 3.—Planar projection (as viewed by an observer in the plane of the sky) of the heliomagnetic latitude at a tilt angle of 30° as a function of solar latitude and longitude. The solid line represents a neutral line as seen in the plane of the sky. P is a point of pB observation in the plane of the sky, and θ_{mg} is the minimum distance of P from the current sheet. Here θ is the heliographic latitude of the source point P.

are not identical, we cannot determine the heliomagnetic latitude, θ_{mg}, simply by using equation (2). We define an additional angular parameter, θ_{min}, which is a measure of the minimim angular distance between the point of a pB observation and the neutral line as it appears in a synoptic map. Thus, whenever we use observed pB data, we use θ_{min} to represent the distance of a coronal source point from the inferred neutral line, and for all calculated values of pB (using electron density models, as discussed in § 4), we use θ_{mg} to represent the distance from the heliomagnetic equator (neutral line).

3. CORONAL pB OBSERVATIONS AND THE CURRENT SHEET

3.1. *Organization of pB Data with Respect to* θ_{min}

We now consider the variation of pB with respect to the parameter θ_{min}, for each height, within a given epoch. Figures 4

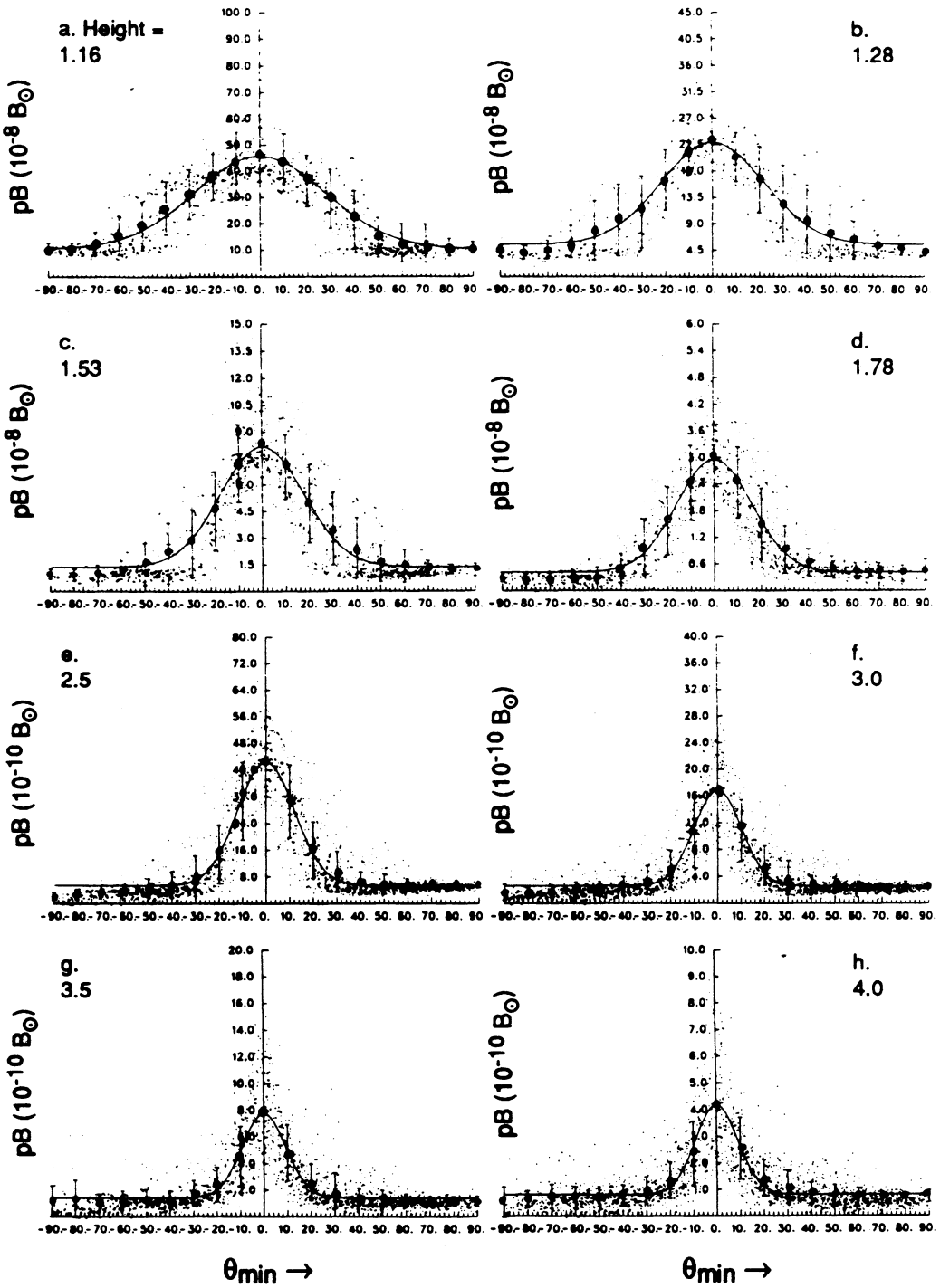

FIG. 4.—Plot of pB values between 1973 day of year (DOY) 337 and 1974 DOY 26, at heights 1.28, 1.78, 2.5, 3.0, 3.5, and 4.0 $R_\odot$ for epoch 1 vs. angular distance θ_{min} from the current sheet. Mean values and their standard deviation are plotted for each 10° interval in θ_{min}.

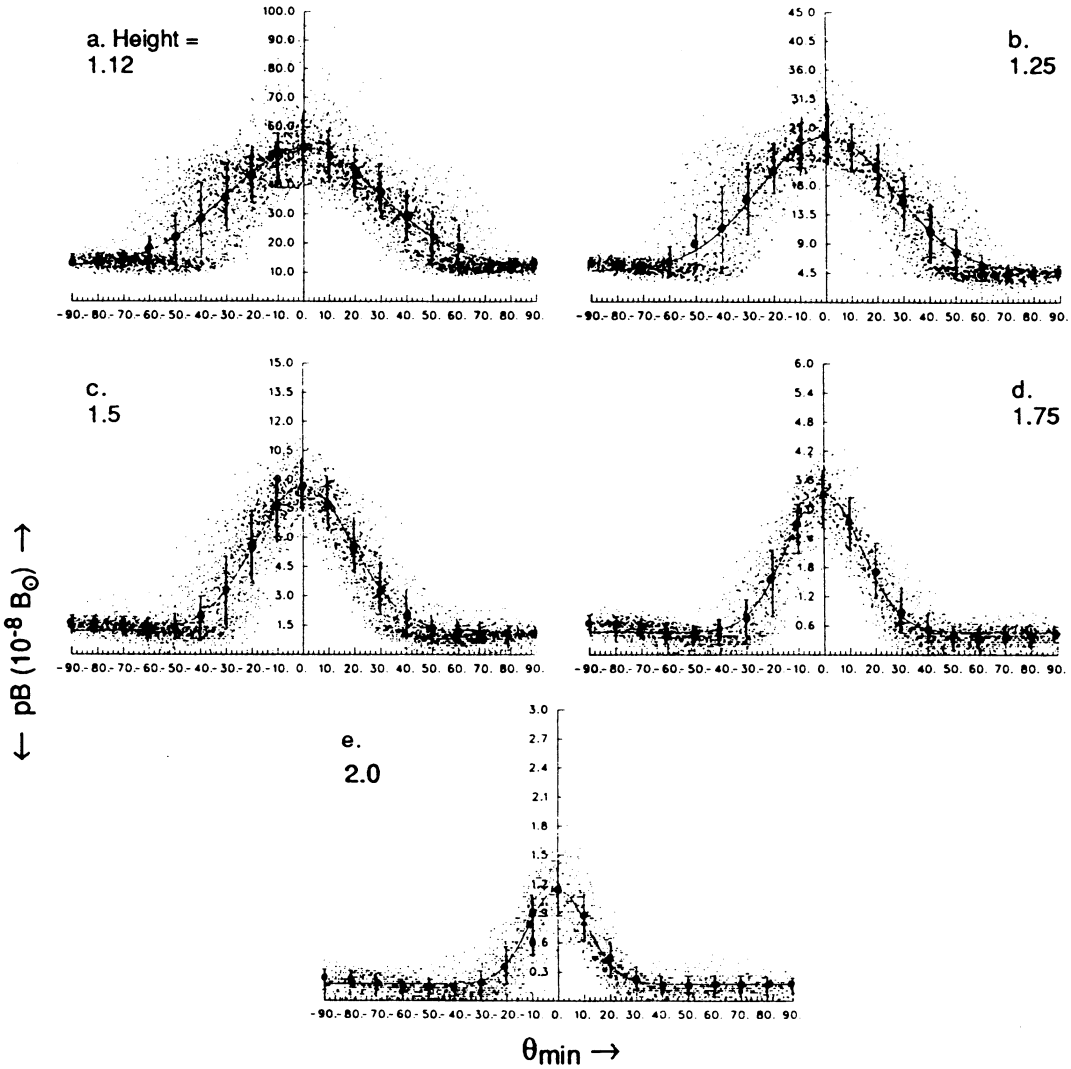

FIG. 5.—Same as Fig. 4, except this is for 1976 DOY 114 and 1976 DOY 276 (epoch 3) at heights 1.12, 1.25, 1.5, 1.75, and 2.0 $R_\odot$

and 5 display the distribution plots of pB as a function of $\theta_{\min}$ for various heights during epochs 1 and 3, respectively. In order to quantify the distribution of pB as a function of $\theta_{\min}$ (for each height), it is convenient to parameterize the distribution. Although the choice of a particular mathematical function is somewhat arbitrary, a Gaussian function plus a constant background at each height fits the distribution quite well. The function is given by

$$pB(\rho, \theta_{\min}) = pB_p(\rho) + [pB_{cs}(\rho) - pB_p(\rho)]e^{-\theta_{\min}^2/w_{pb}^2(\rho)}, \quad (3)$$

and the three parameters fitted to the distributions at each height are $pB_p(\rho)$, polarized brightness at the tail of the Gaussian (the polar holes), $pB_{cs}(\rho)$, polarized brightness at the peak of the Gaussian (in the current sheet), and $w_{pb}(\rho)$, the "half-width" of the distribution.

Here we have used nonlinear least-squares fitting to determine the appropriate values of the parameters of equation (3). The method of least-squares procedure involves minimizing χ^2 with respect to each of the parameters used. From the distribution plots (Figs. 4 and 5) of pB, we observe that the effect of even a few high values of pB (owing to high-latitude structures) in polar regions has a tendency to increase the value of the fitted parameter pB_p compared to the mean value of pB in the region. During epoch 1, the south polar hole was 1.17 times dimmer than the north polar hole, while during epoch 3 the south polar hole was 1.14 times brighter than the north polar hole. Since we are fitting a symmetric Gaussian function with a constant background at a given radial height, the above facts should be taken into consideration. We introduced constraints by fixing the parameter pB_p to be the average of the mean values of the north and south polar regions. This value was obtained the following way: (1) we obtained the mean of the distribution of pB in 10° angular bins, and (2) within each epoch and at each radial height we determined an angular width in the north and south polar regions at which mean pB remained constant to within 15% of the smallest mean obtained at the north and south polar regions at that height, and finally, (3) we obtained an average of these mean values, which was the value chosen for pB_p.

Using this fixed estimate of pB_p, we carried out a two-parameter least-squares fit to the data. Applying this constraint changes the values of pB_{cs} by only $\pm 5\%$, while the change in the half–angular width, w_{pb}, is about $\pm 10\%$. Table 1 contains the values obtained for epoch 1 from the two-

TABLE 1

TWO-PARAMETER GAUSSIAN FIT IN TERMS OF θ_{min} (EPOCH 1)

Height ($R_\odot$) (1)	pB_{cs}[a] (2)	pB_p[a] (3)	w_{pb} (4)	R (5)
1.16.....	457.10(1)	104.20	39.5(3)	0.80
1.28.....	224.10(1)	41.00	34.8(3)	0.80
1.53.....	80.30(1)	10.60	27.0(3)	0.83
1.78.....	29.20(2)	3.20	23.9(2)	0.86
2.0.....	10.10(2)	1.40	18.7(4)	0.81
2.5.....	4.20(1)	0.440	17.9(6)	0.89
3.0.....	1.67(1)	0.223	14.8(5)	0.86
3.5.....	0.76(3)	0.115	14.3(5)	0.81
4.0.....	0.41(4)	0.065	14.2(4)	0.78
4.5.....	0.23(3)	0.040	14.8(4)	0.75
5.0.....	0.15(3)	0.030	14.9(4)	0.52

[a] All polarized brightnesses are in units of 10^{-9} $B_\odot$ (5200 Å). Quantities in parentheses are standard error (in percent) estimates of the respective parameters.

parameter fit in which pB_p is kept fixed, where column (5) provides the correlation coefficients of the fits.

We found on average that values of polar pB_p for epoch 1 were within $\pm 13\%$ of the values of pB_p obtained from epochs 2 and 3, while the pB_{cs} values for epoch 1 were within $\pm 10\%$ of the values for epochs 2 and 3. The half-angular width of the distributions during epoch 1 was 10%–20% larger than that of epochs 2 and 3. Thus, we conclude that pB estimated at the current sheet and above coronal holes displays only minor variations during the descending and minimum phase of the solar cycle, although the scatter in the distribution plots decreases significantly with the approach to solar minimum.

Based on the simple model of a tilted dipolar corona during solar minimum, we defined the following criteria to specify the edge-on position of the current sheet to determine the true value of pB_{cs} at the current sheet and the angular width of the current sheet for a given solar rotation (Fig. 6). First, the two edge-on positions within a given rotation should be separated by approximately 180°; next, the neutral line should be at its maximum latitudinal extent (relative to the heliographic equator); and finally, the width of the profile of pB signal as a function of θ_{min} should be at its minimum, and the magnitude of the pB signal should be maximum (indicated by closed contour lines).

During epoch 1 we find that for a given solar rotation there are no solar longitudes that satisfy all the above criteria, and thus we chose the narrow region (Fig. 1, *top*) consisting of two days (1973 DOY 352 and 353) for rotation 1609 and two days (1974, DOY 16 and 17) for rotation 1610 around $-30°$ latitude which satisfied conditions (2) and (3) above, to determine the magnitude of pB in the current sheet. However, the tilted dipolar nature of the corona is obvious from Figure 6, which shows double peaks in pB about the heliographic equator at latitudes 20° and $-30°$, with the equatorial pB being about a factor of 1.4 lower than the peak pB values. During epoch 3, which represented solar minimum, we were able to satisfy all the above criteria. Analyses for epochs 2 and 3 are presented elsewhere (Guhathakurta 1989). The magnitude of $pB_{cs}(\rho)$ for the few days when the current sheet was viewed edge-on is presented in Table 2, and these values are higher than the average $pB_{cs}(\rho)$ for the entire data presented in Table 1. This does not come as a surprise, since the streamers are the brightest in this orientation because the current sheet is in the plane of the sky at the limb.

3.2. *Results of the pB Analyses*

From the analyses of the pB data we reach the following conclusions:

1. The observed pB value is a maximum when the current sheet is veiwed edge-on and a minimum when the current sheet appears face-on in the plane of the sky. As a result, there is a significant variation in pB values from the mean pB_{cs} obtained at the current sheet (up to $\pm 40\%$ from the mean), even though the uncertainty in individual pB measurements is only $\pm 8\%$. Thus, this is a geometric effect alone. The pB values at the poles vary significantly less from the respective mean values obtained at the poles, even though the uncertainty in individual pB_p measurements is much higher when compared to pB_{cs}. This is so because pB_p is a function of r alone, and the changing geometry as a function of solar rotation has no effect on it. The error bars (showing ± 1 σ) in Figures 4 and 5 express quantitatively the variations from the mean as a function of θ_{min}.
2. In the distribution plots, there appears to be a constant (as a function of θ_{min}) band at each height (the width of the band is approximately 2 σ) of low values of pB over the poles.
3. The angular width of the constant band described above increases with height.

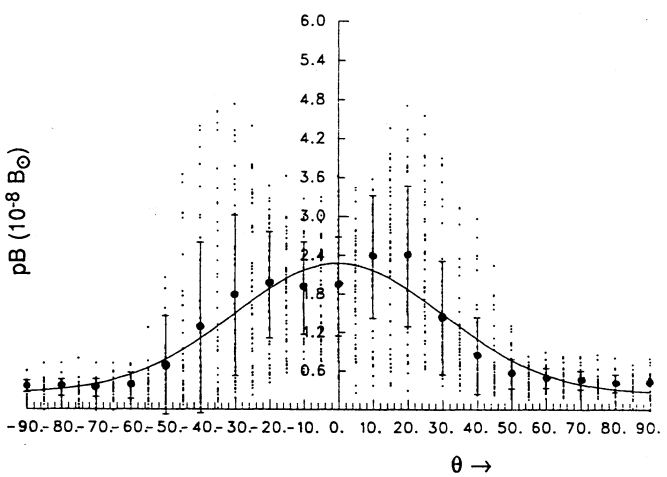

FIG. 6.—Plot of pB values between 1973 DOY 337 and 1974 DOY 26, at height 1.78 $R_\odot$ for epoch 1 vs. heliographic latitide θ. Mean values and their standard deviation plotted for each 10° interval in θ_{min}.

TABLE 2

TWO-PARAMETER GAUSSIAN FIT IN TERMS OF θ_{min} (EPOCH 1) EDGE-ON POSITION

Height	pB_{cs}[a]	w_{pb}
1.16.....	650.00	33.5
1.28.....	306.20	22.7
1.53.....	108.60	15.4
1.78.....	39.20	12.9
2.5.....	6.80	10.4
3.0.....	2.56	9.4
3.5.....	1.11	9.1
4.0.....	0.57	9.2
4.5.....	0.28	9.2
5.0.....	0.18	9.4

[a] Polarized brightnesses are in units of 10^{-9} $B_\odot$ (5200 Å).

Based on the above results, we define coronal holes to be those regions in which the mean of polar pB values remains constant to within $\pm 15\%$ of the smallest mean obtained in that region. Using this definition, we can determine the boundary of the polar coronal hole by solving equation (3) for $\theta_{\min}$ where $pB(\rho, \theta_{\min})$ is equal to $1.15pB_p$, i.e.,

$$\ln\left(\frac{pB_{cs} - pB_p}{0.15pB_p}\right) = \frac{\theta_{\min}^2}{w_{pB}^2} . \quad (4)$$

Thus, organization of the pB data about the current sheet allows us to infer the boundary of the polar coronal holes. However, if we had organized the pB data about the heliographic latitude θ, as in Figure 6 (compared to Fig. 4*d*), then the width of the coronal hole boundary would appear much smaller. In this particular case, the width estimated from Figure 6 is 35°, while that estimated from Figure 4*d* is 45° at a height of 1.78 $R_\odot$. The width and the area of the coronal hole determined by using equation (4) are more than those estimated by Munro & Jackson (1977), and these results are presented elsewhere (Guhathakurta 1992: Guhathakurta & Holzer 1994).

3.3. *Uncertainties and Errors*

The observational data and above procedures are subject to several sources of uncertainties and error. First, uncertainty in the pB distribution plots are caused by (1) the photometric error associated with measurements of pB signals; (2) the error or variance that results from being unable to determine the particular geometry of the system (the effect of the varying geometry of the warped and distorted current sheet as a function of solar rotation on the observed value of pB, along a given line of sight, in the plane of the sky), and (3) temporal evolution and longitudinal lumpiness within a given epoch.

Instrumental error which is random is found to be much higher for the pB values at the poles (15% at 1.2 to 41% at 1.8 $R_\odot$ for Mark II data, and 13% at 2.5 to 82% at 5.0 $R_\odot$ for WLC data) than at the current sheet (up to $\pm 8\%$) (see Guhathakurta 1989). Note that the standard deviation obtained from the distribution plots of pB over the polar holes (Fig. 4) is smaller than the variance in pB resulting from instrumental uncertainty alone. This fact suggests that the scatter in pB values inside the polar holes can be explained by instrumental uncertainty alone, and the variation attributable to temporal evolution, longitudinal lumpiness, or the interpretation of data is masked by this rather large instrumental uncertainty. In the absence of high-latitude features and transients, we can determine the mean value of pB inside the holes with an accuracy of $\pm 7\%$ standard error (Guhathakurta 1989). Thus, the limit on the polar pB variation is $\pm 7\%$ of the mean polar pB value.

The variance in mean pB_{cs} at the current sheet for the entire epoch is much larger than the variance at the poles. Thus, we conclude that the variance in the pB distribution at the current sheet in this particular analysis is mainly attributable to the combined effect of the changing geometry of the current sheet with respect to an observer on the Earth (which provides longitudinal variation in pB), temporal evolution, and instrumental error (in that order). The standard error for mean pB_{cs} is $\pm 4\%$ (Guhathakurta 1989).

4. MODELING THE LARGE-SCALE ELECTRON CORONA

In the previous section we found that for the period 1973–1976, the large-scale pB data were well organized with respect to the minimum angular distance from the current sheet and that the pB distribution inside the polar coronal holes was independent of latitude. The absence of latitudinal variation ($\theta_{\min}$) in the polar holes (within the limits of observational uncertainties with a standard error of $\pm 7\%$) can only imply that the electron density inside the polar holes was also independent of latitudinal variation. Even a small angular variation in electron density inside the holes, as considered by Munro & Jackson (1977), would result in a pB distribution that showed a substantial increase with angle, which was simply not observed (Guhathakurta 1989; Guhathakurta & Holzer 1994). In the heliomagnetic coordinate system (r, θ_{mg}, ϕ_{mg}), the electron density is independent of longitude ϕ_{mg}. Therefore, the electron density in the magnetic equatorial plane of this coordinate system is a function of r only. The reader is reminded that θ_{mg} is a function of θ and ϕ.

The observed quantity pB displayed on the synoptic maps is not a local physical parameter, and its relation to such a quantity as the electron density is through the line-of-sight integral (Billings 1966)

$$pB = \frac{B_\odot R_\odot \pi\sigma}{2(1 - u/3)} \int_{-\infty}^{\infty} N(l)[(1 - u)A + uB] \frac{\rho^2}{r^2}\, dl , \quad (5)$$

where $N(l)$ is the electron density along the line of sight, ρ is the distance of closest approach along the line of sight ($l = 0$ at this point), u is the limb-darkening factor, and σ is the Thompson scattering cross section. A and B are complicated functions of r describing the changing geometric relationship between the radius vector from the Sun and the direction of the observer.

Now we have a set of data points pB as a function of height ρ, position angle η, and longitude L which measure the coronal polarized brightness along the line of sight through the corona according to equation (5), and we look for ways to invert the integral equation (6) below in a semianalytic manner to obtain electron density N as a function of r and θ_{mg}. However, one of the issues is when to determine the density of the current sheet. When the streamer belt is edge-on in the plane of the sky, the polarized brightness is a maximum. In this case, the coronagraph is looking along the streamer belt; i.e., where all the streamers are at the same latitude behind each other along the line of sight, and they all contribute to the observed pB. Thus, the observed brightness is greatest because of geometric effects alone. The density derived in this geometry does not tell what the derived density is from a perspective looking perpendicularly through the current sheet, which is most directly related to the density in the current sheet. However, during solar minimum there are typically two equatorial streamers on the two limbs of the Sun. Thus, when these streamers are edge-on in the plane of the sky, we are picking up contributions from one streamer only. In our analysis, we chose the edge-on pB value to estimate electron density at the current sheet. In § 4.4 a short discussion is provided on how this density would vary if we chose the average pB or the pB obtained when the current sheet is face-on in the plane of the sky.

Since pB over the heliomagnetic poles and in the current sheet is a function of r only, we can invert the integral equation (6) for these two position angles in an analytic fashion, following the technique used by van de Hulst (1950) to obtain the electron density over the poles and in the current sheet.

If electron density is a function of r only, we can write the polarization brightness in the form

$$pB(\rho) = \frac{B_\odot R_\odot \pi\sigma}{1 - u/3} \int_{\rho}^{\infty} N(r)[(1 - u)A + uB] \frac{\rho^2}{r^2} \frac{r\, dr}{(r^2 - \rho^2)^{1/2}} . \quad (6)$$

If the pB signals are expressed as a polynominal,

$$pB(\rho) = \Sigma a_i \rho^{-b_i}, \quad (7)$$

then the electron density can be written as

$$N(r) = \frac{\Sigma \alpha_i(a_i, b_i) r^{-\beta_i}}{[(1-u)A + uB]}. \quad (8)$$

Here the coefficients a_i and b_i are obtained by using a minimizing technique to reproduce the measured pB values to within $\pm 5\%$, and α_i and β_i are determined from the a_i and b_i values (Guhathakurta 1989). The electron density is then expressed in the form

$$N(r) = \Sigma c_i r^{-d_i}, \quad (9)$$

where c_i and d_i are obtained again by using a minimizing technique. Here we shall provide modeling analysis only for epoch 1; the analyses for epochs 2 and 3 are presented elsewhere (Guhathakurta 1989, 1994). Tables 3A–3C list the coefficients of the power-law expression used to fit the observed pB data at the current sheet for epoch 1, observed pB data at the current sheet for the edge-on position of the current sheet, and the pB data observed at the heliomagnetic poles, respectively. The above functions reproduce observed pB values to within $\pm 5\%$. Table 3B lists the coefficients of the power-law expression for the subsequent electron density models obtained by using the parameters in Table 3A. From the preceding discussions here and in § 3, we come to the conclusion that the electron density inside the polar coronal holes remains constant with magnetic latitude and longitude and the angular width of the holes increases with height (Guhathakurta & Holzer 1994). A suitable functional form representing the electron density in the heliomagnetic coordinate system as a function of latitude is

$$N(r, \theta_{mg}) = N_p(r) + [N_{cs}(r) - N_p(r)]e^{-\theta_{mg}^2/w^2(r)}, \quad (10)$$

where the value θ_{mg} in equation (10) is given by equation (2). Here $N_p(r)$ represents the density inside the holes and $N_{cs}(r)$ represents the density at the current sheet for edge-on orientation. The parameter w represents the half-angular width of the current sheet at which the electron density (or the polarized brightness) reduces to half its maximum value observed in the edge-on position of the current sheet (this parameter is the same as w_{pb} of Table 2). A functional form for w is obtained by fitting a polynomial of the form $\Sigma \gamma_i r^{-\delta_i}$ and then solving for γ_i and δ_i (Table 3C). The half-width of the current sheet, w, gives a measure of the angular width of the coronal holes. At a given distance r, for θ_{mg} far greater than w the density is a constant with respect to θ_{mg} and is equal to $N_p(r)$.

The success of any model is partially demonstrated by its ability to reproduce the observed quantities. In our case, this would mean reproducing the three parameters fitted to the observed pB data when the current sheet was oriented edge-on in the plane of the sky (Table 2) and also reproducing the three parameters when the entire epoch 1 was considered (Table 1).

4.1. *Calculated pB Using the Density Model*

We have plotted (Fig. 7*a*) the calculated pB at the current sheet and at the poles for the edge-on orientation of the current sheet for epoch 1, while the corresponding values obtained from the observed pB distribution for all three epochs are over plotted. In Figure 7*b* we plotted the half-angular width w for all three epochs. The agreement between the model pB parameters and the observed pB parameters is better than $\pm 7\%$; these results are given in Figure 8 for epoch 1. Figure 9 presents the calculated pB distribution plot and the corresponding synoptic map for height 2.5 $R_\odot$. We used the observed values of $\alpha = 30$ and w from Table 2 to calculate pB.

4.2. *Sensitivity Study*

How sensitive is the electron density model to parameters like the half-angular width w and the shape of the neutral line? First we consider the calculated pB as function of w.

We select two profiles to cover the broad spectrum of the half-width w of the current sheet. Profile w_1 is chosen on the basis of the half-angular width w_{pb} (Table 1). This profile represents an average width during the given period and thus provides an upper limit to the half-angular width w. Profile w_2

TABLE 3

COEFFICIENTS OF POWER LAWS

A. pB

pB Model	a_1	b_1	a_2	b_2	a_3	b_3
Current sheet (average)	1.06	4.17	6.52	6.90	4.22	6.84
Current sheet (edge-on)	3.92	5.0	5.67	5.95	11.06	11.26
Poles	0.03	3.24	0.10	4.08	3.67	9.17

B. $N_e(r)$

Density Model	c_1	d_1	c_2	d_2	c_3	d_3
Current sheet (average)	1.07	3.1	19.94	6.06	22.10	12.93
Current sheet (edge-on)	1.41	3.39	16.42	5.14	61.90	12.67
Poles	0.14	2.8	8.02	8.45	8.12	16.87

C. $W(r)$

Model	γ_1	δ_1	γ_2	δ_2	γ_3	δ_3
w1	26.9	0.5	31.1	5.13	0.01	5.49
w2	11.1	0.7	4.73	6.00	10.00	6.14
w	16.3	0.5	10.0	7.31	43.20	7.52

NOTE.—All coefficients a_i, c_i, and γ_i are in units of 10^{-7}, 10^7, and degrees, respectively.

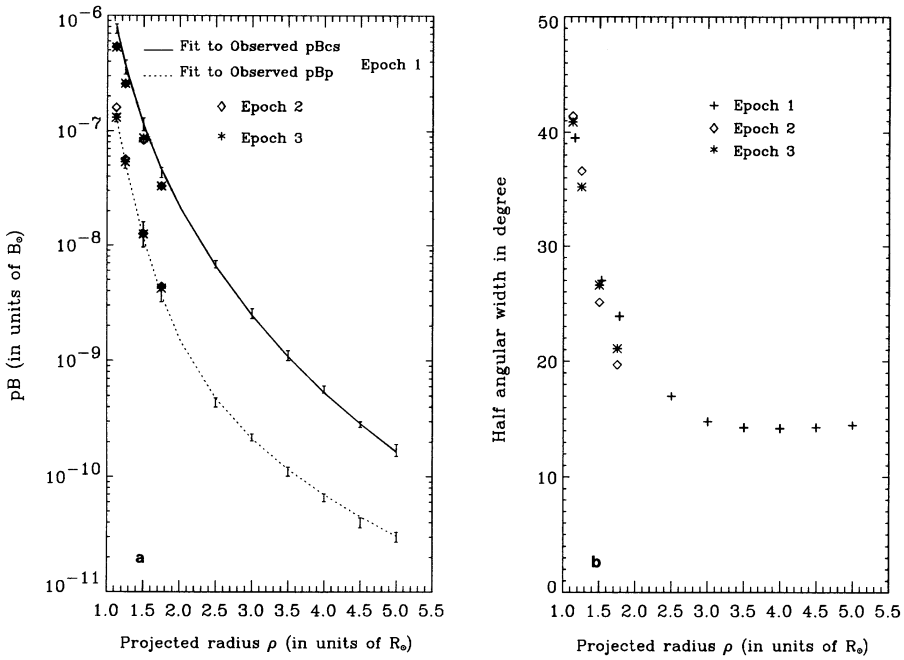

FIG. 7.—(*a*) Comparison of pB_{cs} and pB_p values (obtained from the two-parameter fit) for the three epochs. (*b*) Comparison of w_{pb} values (obtained from the two-parameter fit) for the three epochs.

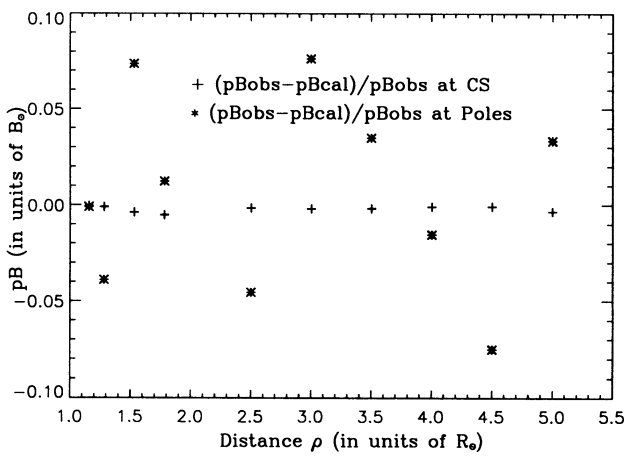

FIG. 8.—Difference plot of pB observed vs. pB calculated using the density model parameters from Table 3B and half width w for the current sheet (*plus signs*) and at the poles (*stars*).

represents the half-angular width at which the observed pB values is roughly 0.9 times its maximum value, making the width extremely narrow. This profile provides the lower limit to w. Profile w is the observed profile (Table 2) during the edge-on position of the current sheet, which is in between w_1 and w_2. The three profiles w_1, w_2, and w are plotted in Figure 10. The functional form used to describe the profiles of w is as described before in § 4, and the coefficients are presented in Table 3C. Using w_1 in the density model has the effect of increasing the values of the parameters pB_{cs} by 20% and the corresponding w_{pb} by 40% as compared to the use of w. However, using w_2 reduces the values of the parameters pB_{cs} by up to 30% and the corresponding w_{pb} by up to 60% when compared to the use of w. Thus, using the upper limit w_1 for the half-width of the electron density model has an overall effect of increasing the values of the two parameters, while using the lower limit w_2 has an overall effect of reducing the values of the two parameters relative to the values that are obtained by using w. The essence of the preceding discussion is captured in Figure 11.

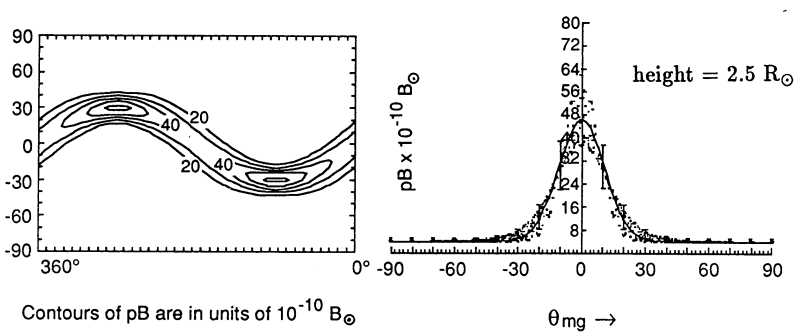

FIG. 9.—Contour and distribution plots of a calculated pB at height 2.5 $R_\odot$, for $\alpha = 30°$

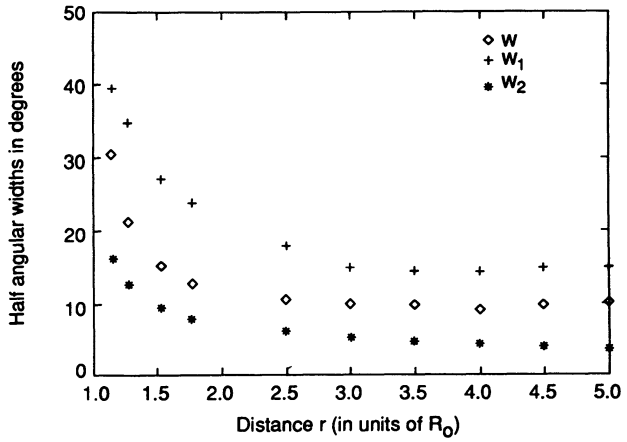

FIG. 10.—Plot of half-widths w, w_1, and w_2

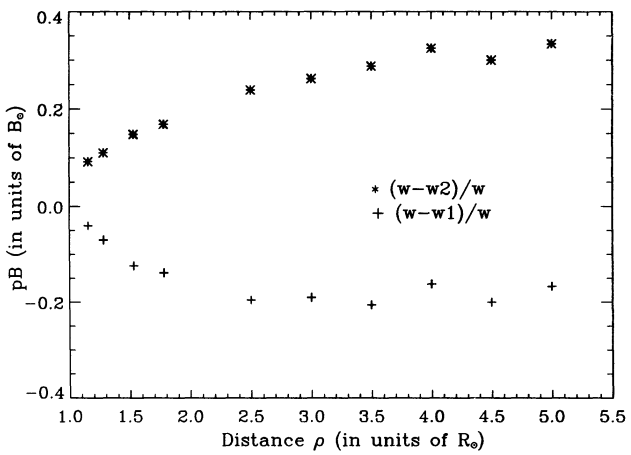

FIG. 11.—Difference plot of $pB_{cs}(w)$ calculated using the density model parameters from Table 3B vs. pB_{cs} calculated using $w1$ and $w2$ as half-widths.

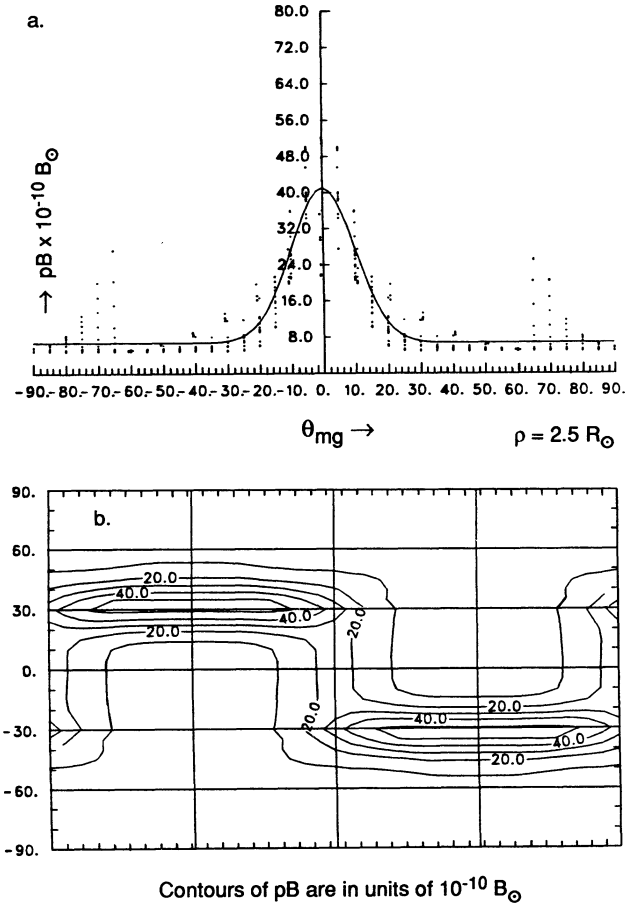

FIG. 12.—Distribution and contour plot of calculated pB (using a current sheet that traces a square wave as the neutral line in the plane of the sky) vs. θ_{mg} at height 2.5 $R_\odot$ and $\alpha = 30°$. The fitted parameters are 45.0 × 10^{-10} $B_\odot$ and 14°1. Contour levels are in the range from 20–80 × 10^{-10} $B_\odot$.

Next we examine the sensitivity of the calculated pB to the shape of the inferred neutral line. Note that the neutral line from epoch 1 is a profile whose shape is between a sinusoidal curve and a square wave. However, all the calculations we have performed so far assume a neutral line whose profile is represented in Figure 3. Thus, it is useful to examine any effect of the assumed shape on the model electron density. The calculated distribution plot and the synoptic map obtained for a square-wave neutral line is plotted in Figure 12.

The discontinuity in the current sheet at 0° and 180° for the square wave neutral line causes numerical problems for computations of pB which then causes the contours to be distorted in the vicinity of these longitudes, thereby giving rise to the peaks around ±70° from the neutral line. This is just an artifact of the numerical problem and has nothing to do with the latitudinal dependence of pB in the holes. Even for such a physically unreasonable case, we can draw some basic conclusions. The values of the parameters pB_{cs} obtained along the current sheet using the square wave neutral line are within ±5% of the parameter pB_{cs} (Table 3A, row 2) obtained by using a sinusoidal neutral line. Thus, the effect of the shape of the neutral line in estimating $N_{cs}(r)$ is negligible. The most important difference found from using a square wave neutral line is the overall increase in the scatter obtained in the distribution plots of the calculated pB data. Thus, the effect of changing the shape of the neutral line (maintaining the same tilt angle) is to increase the overall scatter in the distribution plots of pB as a function of θ_{min}.

4.3. *Analyses of the Results*

From the study in § 4.1 we observe that a sinusoidal neutral line reproduces all the observed parameters within an accuracy of ±7% but cannot reproduce all the observed scatter in the distribution plots, especially at low heights. A much larger overall scatter results from using a square wave neutral line, as shown in the preceding section. The distribution plots of the observed data show large scatter at low heights (1.2–1.5 $R_\odot$) in the corona which are mostly attributable to the temporal evolution of the small-scale features in the corona and to the nonsinusoidal nature of the neutral line geometry. This is also evidenced in the neutral line profiles at low heights. With increased height, the large-scale structure of the corona dominates, and it is because of the geometry of the system that we observe scatter in the distribution plots of the observed data (as shown in Figs. 4 and 5, where the organization with respect to the current sheet improves in the outer corona). This model does not reproduce the scatter observed at low heights that is associated with the evolution of the small-scale features but reproduces quite well the scatter seen at higher altitudes which is primarily caused by the effect of the changing geometry of the system.

The error in inferred electron densities is larger than the standard error estimated from *pB* observations because the electron density is obtained by deconvolving the observed *pB* values. By ascribing uncertainties to the a_i' and b_i' values and using equation (8), we estimate the uncertainty in the electron density values to be $\pm 15\%$ at the poles and $\pm 11\%$ at the equator. The radial gradient of the *pB* measurements (and therefore the electron density) is uncertain to the extent the cross calibration coefficient is uncertain.

4.4. *Model Comparisons*

The organization of the *pB* data into a geometry of the corona that is appropriate for the magnetic geometry guarantees that the resultant electron densities will be greater than those based upon solar coordinates. Thus, we expect differences between the present model and past work owing to the selection effect inherent in this work.

We initially compare our two-dimensional empirical model of the quiet Sun with the two-dimensional model proposed by Saito (1970). The latitudinal variation of the Saito (1970) model is quite different from ours and is best compared via Figure 13. The difference in the shape of the latitudinal profile probably comes from averaging the data in latitude bins with respect to the solar rotation axis. The low polar value might be attributable to an absolute calibration difference. The spherically symmetric polar density model of Saito does not match any of the polar models we discuss later in this section.

The equatorial density values obtained from the models of Allen (1973) and Newkirk (1967) are much lower (by factors of 2.8 and 2.1, respectively) than our density values obtained at the current sheet because of the different distributions of density considered by these models. Disagreements may also have resulted from the absolute calibration differences of different data sets used in these studies. Allen (1973) and Newkirk (1967) models were obtained for the solar minimum corona. In Figure 14 we have plotted the electron density values at the equator for all the models discussed.

Comparison of our model with that of Saito et al. (1977) is of special interest because they used the same calibrated data set (from *Skylab*) and for the same phase of the solar cycle as we did. The background equatorial density values obtained from the model by Saito et al. (1977) is a factor of 2.4 lower than our

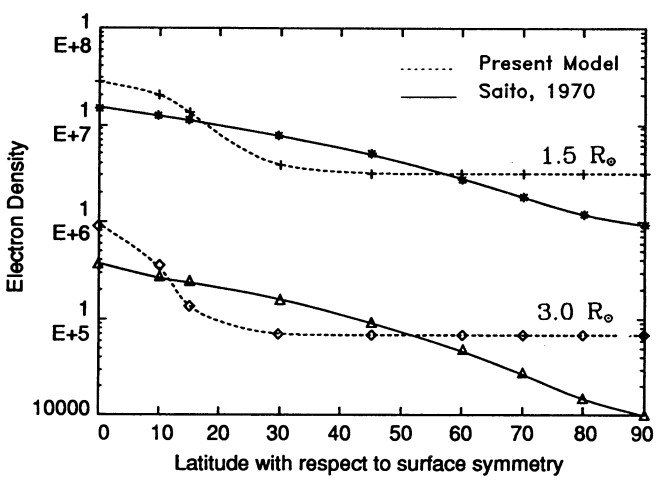

FIG. 13.—*Solid line:* Electron density as a function of heliographic latitude for the Saito (1970) model at heights 1.5 and 3.0 $R_\odot$. *Dashed line:* Electron density as a function of heliomagnetic latitude using the current sheet model at heights 1.5 and 3.0 $R_\odot$.

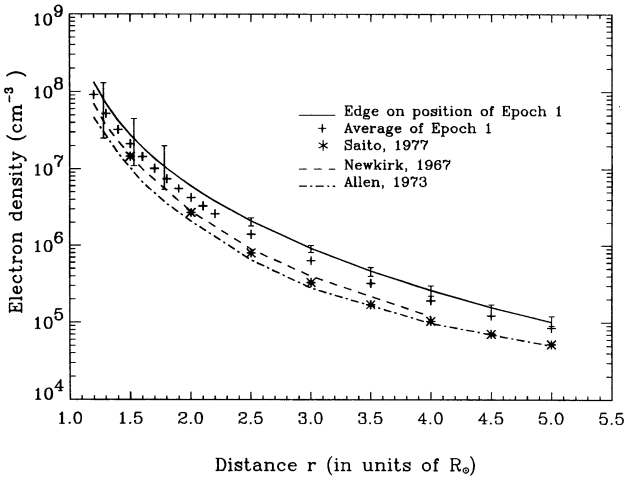

FIG. 14.—Electron density as a function of radius. Densities obtained at the current sheet from the present work (*vertical lines*), Saito (1977) equatorial model (*stars*), Newkirk (1967) equatorial model (*dashed line*), Allen (1973) equatorial model (*dot-dashed line*), and the adopted relationship for the density along the current sheet during epoch 1 (*solid line*).

density values obtained at the current sheet. This difference arises primarily from using two different distributions to represent the electron density and, to a smaller extent, from the two different time periods considered by these two models. Saito et al. (1977) used 10 days' worth of data (5 days centered around each DOY 286 and DOY 283 during 1973) when no streamers or holes were visible on the limb, and then they averaged the observed data obtained at the equator. We, on the other hand, isolated days (over a period of two solar rotations) when the perpendicular to the current sheet lay in the plane of the sky, and we averaged the data obtained at the neutral line during those days. The polar density values obtained from the spherically symmetric case of the model by Saito et al. (1977) is within $\pm 4\%$, and this difference is not considered significant.

For the same period (1973 June 29 through July 13), Munro & Jackson (1977) carried out an analysis of the electron density of a north polar coronal hole using the *Skylab* data. When compared to our density values at the poles, the MJ polar values are a factor of 1.42 lower. In the MJ axisymmetric model of the coronal hole, the latitudinal variation of the electron density inside the hole was used to match the observed *pB* values at the poles. This latitudinal distribution required the density directly over the pole to be about a factor of 1.3 lower than that derived for the spherically symmetric polar model of Saito et al. (1977). The values obtained from the MJ spherically symmetric polar model are within $\pm 9\%$ of our values, and this difference is likely attributable to different time periods considered.

The polar minimum model of Allen (1973) results in density values that are about a factor of 1.45 lower than our density values. Such a large factor can be explained by considering the absolute calibration differences in the two data sets. We have observed that the ATM (*Skylab*) data set was brighter by a factor of about 2 when compared to the Coronal Camera measurements of the eclipse of 1973 (Lilliequist 1977). Thus, if we had calibrated our data in the same unit as that of the Coronal Camera data set, then the density at the poles would be a factor of 0.7 times lower than the Allen (1973) values. Figure 15 presents the comparison of all the polar models discussed.

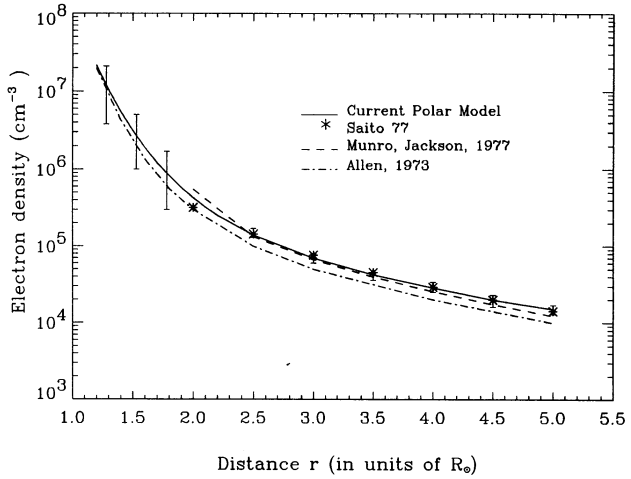

FIG. 15.—Electron density as a function of radius. Densities obtained at the polar hole region from the present work (*vertical lines*), the Saito (1977) spherically symmetric polar model (*stars*), the Munro-Jackson (1977) polar model (*dashed line*), the Allen (1973) polar model (*dot-dashed line*), and the adopted relationship for the density at the poles during epoch 1 (*solid line*).

From § 3.2, we found that the *pB* observed with the streamer being edge-on/face-on in the plane of the sky is about +40% brighter and 30% dimmer than the average *pB* at the current sheet for the entire rotation. Thus, our current sheet models would be reduced by roughly a factor of 1.4 if we chose average *pB* to estimate electron density (as done by previous modelers), bringing them in closer agreement with the previous equatorial models.

5. SUMMARY AND CONCLUSIONS

In this study we have employed the white-light coronagraph observations from the K-coronameter and the ATM (aboard *Skylab*) to describe the large-scale three-dimensional density structure of the corona in terms of organization by an inferred current sheet (heliomagnetic "equator"), at a time of low solar activity and small coronal changes. In our analysis we have emphasized a simple relationship between *pB* values and the large-scale magnetic field as observed from these data, where bright coronal regions identified with closed magnetic geometry have decreasing angular widths at increasing heights following the boundaries of the polar coronal holes.

Our main conclusions may be summarized as follows:

1. The *pB* scans are far better organized in terms of θ_{min} (Figs. 4 and 5), in which the magnetic dipole axis furnished the axis of symmetry during the descending and minimum phase of the solar cycle, than the heliographic latitude (Fig. 6). This organization permits a quantification of *pB* (eq. [3]), applicable during the last third of the solar cycle.

2. As radial distance increases, the large-scale structure of the corona dominates. The variation in the observed *pB* signal in the current sheet is primarily caused by the changing geometry of the system. On the other hand, the variation in the observed *pB* signal in the polar region is principally a result of noise.

3. A broad minimum is observed from the *pB* scans over the polar holes, and the width of the polar coronal holes increases with height. For the same radial height, the width in "θ_{min}" of the coronal hole boundary is greater than that obtained in terms of the heliographic latitude "θ" (§ 3.1).

4. No systematic variation in *pB* at the current sheet or in the polar holes occurs within the declining phase of the solar cycle. In the polar regions, no variations above the sensitivity of the instruments ($\pm$13% at 2.5 $R_\odot$ and $\pm$82% at 5.0 $R_\odot$) are observed. By averaging over an extended period of time, we are able to reduce the instrumental noise down to $\pm$7% standard error in the polar *pB* measurements.

5. Using the quantitative description of *pB* (eq. [3]), we obtain a quantitative formulation of the electron density in three dimensions during the declining phase of the solar cycle.

The large difference between our current sheet density and other equatorial models can be explained by geometric effects alone. We obtained pB_{cs} when the streamer belt was in the plane of the sky and thus had maximum depth along the line of sight.

We have been able to reduce the uncertainties in the observationally inferred electron density above the poles and at the current sheet and the geometry of the coronal hole by utilizing *pB* data over an extended period of time. The results presented here make it clear that the best quantitative use of the K-coronal *pB* data for determining large-scale density should make use of the organization of the plasma about the current sheet. In future extrapolation of density using this method may be improved further by using data with lower intrinsic noise such as can be expected from the *SOHO* mission.

The physical basis for the solar corona remains one of the central questions in solar physics. Although Parker (1958, 1963) provided the basic physics of the solar wind, there are still many unresolved problems associated with it (Habbal et al. 1994). One of the more promising approaches to resolve some of these issues is through the application of empirical constraints to solar wind models. In one such model (Habbal et al. 1995), the flow properties of the solar wind were derived from a two-fluid model with constraints from one-dimensional white-light density inside a polar coronal hole and in situ interplanetary observations, and the results agreed remarkably well with observations at 1 AU as well as at the base of the Sun. Thus, the usefulness of providing a high-quality density constraint toward the understanding of the solar corona and the solar wind is provided by the Habbal et al. (1995) model. The present three-dimensional model should prove very useful for better understanding of the global hydromagnetic structure of the corona and the solar wind, relating as it does to the magnetic structure of the corona, as opposed to heliocentric coordinates.

Most of this research was supported under a graduate assistantship provided to one of us (M. G.) by the National Center for Atmospheric Research, which is funded by the National Science Foundation, and a small part was supported by the Menzel Fellowship from University of Denver and NASA grant NAG 5-633 to University of Colorado. M. G. would like to thank Victor Tisone and Alice Lecinski for help with Mark II K-coronameter and *Skylab* data reduction, respectively, and also thanks to Gary Rottman, Frank Orrall, Richard Munro, and Arthur Hundhausen for many helpful discussions during the course of the work.

REFERENCES

Allen, C. W. 1973, Astrophysical Quantities (London: Athlone)
Altschuler, M. D., & Newkirk, G. A., Jr. 1969, Sol. Phys., 9, 131
Altschuler, M. D., & Perry, M. R. 1971, Sol. Phys., 23, 410
Behanon, K. W., Burlaga, L. R., & Hundhausen, A. J. 1983, J. Geophys. Res., 88, 7837
Billings, D. E. 1966, A Guide to the Solar Corona (New York: Academic)
Bruno, R., Burlaga, L. F., & Hundhausen, A. J. 1982, J. Geophys. Res., 87, 10339
Fisher, R. R., Garcia, C., Lundin, E., Seagraves, P., Sime, D., & Rock, K. 1985, The White Light Solar Corona, An Atlas of 1984 K-Coronameter Synoptic Charts December 1983–January 1985 (NCAR Technical Note NCAR/TN-246+STR)
Guhathakurta, M. 1989, Ph.D. thesis, Univ. Denver; LASP/Univ. Colorado cooperative thesis
———. 1992, in Proc. SOHO Workshop (ESA SP-348), 109
———. 1994, in Solar Coronal Structures, ed. V. Rusin, P. Heinzel, & J. C. Vial (Bratislava: VEDA Publishing Company), 427
Guhathakurta, M., & Holzer, T. E. 1994, ApJ, 426, 782
Habbal, S. R., Esser, R., Guhathakurta, M., & Fisher, R. 1994, in Proc. Third SOHO Workshop (ESA SP-373), 211
———. 1995, Geophys. Res. Lett., 22, 12, 1465
Hansen, S. F., Sawyer, C., & Hansen, R. T. 1974, J. Geophys. Res., 1, 13
Hoeksema, J. T. 1984, Ph.D. thesis, Stanford Univ.
Hoeksema, J. T., Wilcox, J. M., & Scherrer, P. H. 1982, J. Geophys. Res., 87, 10331
Howard, R. A., & Koomen, M. J. 1974, Sol. Phys., 37, 469
Hundhausen, A. J. 1977, in Coronal Holes and High Speed Streams, ed. J. Zirker (Boulder: Colorado Assoc. Univ. Press), 225
Jokipii, J. R., & Thomas, B. 1981, ApJ, 243, 1115
Levine, R. H. 1977, in Coronal Holes and High Speed Wind Streams, ed. J. Zirker (Boulder: Colorado Assoc. Univ. Press), 103
Lilliequist, C. 1977, Photometry and Polarimetry of the Solar Corona of 30 June 1973 (NCAR Technical Note, NCAR/TN-128+str.)
MacQueen, R. M., Gosling, J. T., Hildner, R. H., Munro, R. H., Poland, A. I., & Ross, C. L. 1974, Proc. SPIE, 44, 207
Munro, R. H. 1985, private communication
Munro, R. H., & Jackson, B. V. 1977, ApJ, 213, 874
Newkirk, G. A., Jr. 1967, ARA&A, 5, 213
———. 1972, in Solar Wind, ed. C. P. Sonett, P. J. Coleman, & J. M. Wilcox (NASA SP 308), 11
Parker, E. N. 1958, ApJ, 128, 644
———. 1963, Interplanetary Dynamical Processes (New York: Interscience)
Perry, R. M., & Altschuler, M. D. 1973, Sol. Phys., 28, 435
Pneuman, G. W., Hansen, S. F., & Hansen, R. T. 1978, Sol. Phys., 59, 313
Saito, K. 1970, Ann. Tokyo Astron. Obs., Ser. 2, 53
Saito, K., Poland, A. I., & Munro, R. H. 1977, Sol. Phys., 55, 121
Schatten, K. H., Wilcox, J. M., & Ness, N. F. 1969, Sol. Phys., 6, 442
Schultz, M. 1973, Ap&SS, 24, 37
Shklovskii, I. S. 1965, Physics of the Solar Corona (2d ed., New York: Pergamon)
Thomas, B. T., & Smith, E. J. 1981, J. Geophys. Res., 86, 11, 105
van de Hulst, H. C. 1950, Bull. Astron. Inst. Netherlands, 11, 135
Wang, Y. M., & Sheeley, N. R. 1992, ApJ, 392, 310
Wilcox, J. M., & Hundhausen, A. J. 1983, J. Geophys. Res., 88, 8095
Wilson, D. C. 1977, Ph.D. thesis, Univ. Colorado; NCAR Cooperative Thesis No. 40
Zhao, Xue-pu, & Hundhausen, A. J. 1981, J. Geophys. Res., 86, 5423
———. 1983, J. Geophys. Res., 88, 451
Zirker, J. 1977, in Coronal Holes and High Speed Wind Streams, ed. J. Zirker (Boulder: Colorado Assoc. Univ. Press), 1